

Site-Selective In Situ Grown Calcium Carbonate Micromodels with Tunable Geometry, Porosity, and Wettability

Seung Goo Lee, Hyundo Lee, Ankur Gupta, Sehoon Chang, and Patrick S. Doyle*

Micromodels with simplified porous microfluidic systems are widely used to mimic the underground oil-reservoir environment for multiphase flow studies, enhanced oil recovery, and reservoir network mapping. However, previous micromodels cannot replicate the length scales and geochemistry of carbonate because of their material limitations. Here a simple method is introduced to create calcium carbonate (CaCO_3) micromodels composed of in situ grown CaCO_3 . CaCO_3 nanoparticles/polymer composite microstructures are built in microfluidic channels by photopatterning, and CaCO_3 nanoparticles are selectively grown in situ from these microstructures by supplying Ca^{2+} , CO_3^{2-} ions rich, supersaturated solutions. This approach enables us to fabricate synthetic CaCO_3 reservoir micromodels having dynamically tunable geometries with submicrometer pore-length scales and controlled wettability. Using this new method, acid fracturing and an immiscible fluid displacement process are demonstrated used in real oil field applications to visualize pore-scale fluid-carbonate interactions in real time.

1. Introduction

Micromodels are artificial transparent porous media that provide direct visualization of a complex flow environment and can be modified to affect porosity, permeability, or wettability.^[1–6] Micromodels have been increasingly used to understand multiphase fluid behaviors and interactions among oil–water–rock phases in underground oil reservoirs. Researchers have recently developed synthetic micromodels through top-down and bottom-up approaches. Various fabrication methods combined with top-down etching or lithographic techniques can achieve geometric representation of the reservoir pores.^[7–15] There have also been significant improvements in posttreatment methods

to modify wettability within micromodels to mimic the reservoir's wettability.^[16–19] Previous micromodels have mostly been made of glass,^[7,8] silicon,^[9,19] and polymeric materials^[10–18] instead of real rock.^[20,21] As a result, they have limitations in studying geochemical fluid–rock interactions, such as acid fracturing to increase the oil production from carbonate reservoirs^[22,23] or changes in wettability due to aging or adsorption of molecules added during simulated enhanced oil recovery (EOR). Features have been wet etched^[20] and laser machined^[21] directly into rock samples and then sealed to make micromodels. These top-down approaches result in large ($\approx 100\ \mu\text{m}$) and relatively simple features. By comparison, microporosity (pore throats and channels $< 10\ \mu\text{m}$) comprises up to 50% of the total porosity in the Ghawar Arab-D carbonate reservoir

(the largest collection of carbonate reservoirs in the world) and critically affects the oil recovery.^[24,25] A simple and controllable method that enables creation of patterned, large-area real rocks with smaller pore-length scales in the microfluidic channels is thus a desirable goal.

Bottom-up strategies inspired by biomineralization have received special attention as a key technology to understand formation mechanism of inorganic materials in nature and to prepare precipitations in synthetic systems.^[26–29] There have been reports on the fabrication of complex carbonate structures via organic templates and a wide range of synthetic methods such as vapor^[30–38] or double diffusions,^[39] and Kitano methods.^[40] Simple reaction-diffusion processes can also generate hierarchical nano- and microstructures.^[41,42] These studies indicate that control over the microenvironments, epitaxy, and inorganic or organic precursors plays an important role in the formation of minerals.^[30–44] Most bottom-up fabrication methods involve both homogeneous and heterogeneous nucleation, and growth processes in solutions and on templates, which result in inevitable problems of undesirable mineralization on channel walls and blocking of the channel.^[45–47] For these reasons, the previous methods cannot be applied to fabricate carbonate micromodels with complex features. In addition, preparing the template fully covered with carbonate requires an additional nucleation process and long process time because negatively charged organic molecules (e.g., acidic polymers) of the template can act as inhibitors of mineral deposition.^[48–50] Therefore,

Dr. S. G. Lee, A. Gupta, Prof. P. S. Doyle
Department of Chemical Engineering
Massachusetts Institute of Technology
Cambridge, MA 02139, USA
E-mail: pdoyle@mit.edu

H. Lee
Department of Mechanical Engineering
Massachusetts Institute of Technology
Cambridge, MA 02139, USA

Dr. S. Chang
Aramco Services Company
Aramco Research Center – Boston
Cambridge, MA 02139, USA



DOI: 10.1002/adfm.201600573

to induce the selective and efficient growth of calcium carbonate within our templates, we eliminated the need for a nucleation step by blending carbonate seed crystals into the noncharged polymeric template. By providing the system with ions rich/supersaturated solutions, these seed crystals grow in size within the templates. Here we report a new bottom-up approach for achieving quasi-2D porous calcium carbonate (CaCO_3) micro-models. CaCO_3 nanoparticles/polymer composite microstructures were fabricated by a photolithographic technique, and by a subsequent in situ growth of CaCO_3 . This approach allows us to quickly create large-area, and tunable CaCO_3 microfluidic test beds capable of accessing a range of topographies and geochemical properties for fundamental studies in geology and reservoir engineering.

2. Results and Discussion

2.1. Fabrication

Our experimental procedure is illustrated in Figure 1a, which can be largely divided into two parts. The first key part is microstructure synthesis in initially empty microfluidic channels using microscope-based photolithography.^[14,51] The surface of the glass microchannel was treated with 3-(trimethoxysilyl)propyl acrylate to fix the polymerized structures on the top and bottom surfaces of the microchannel. In parallel, we ultrasonicated aqueous precursor solutions containing a crosslinker (poly(ethylene glycol) diacrylate), a photoinitiator, a porogen (poly(ethylene glycol)), and CaCO_3 (calcite) nanoparticles. A homogeneous dispersion was needed to reduce the light scattering during UV exposure, and the porogen was added to facilitate the fast diffusion of ions into the polymerized structure (Table S3, Supporting Information). Calcite nanoparticles were used as seed crystals because of their polymorphic stability and well-known growth mechanisms.^[52] The well-dispersed precursor solutions were injected into the acrylate-functionalized microchannel, followed by UV photolithography using a photomask containing desired geometric shapes inserted into the field stop of an inverted microscope. After synthesizing microstructured posts, any uncured precursor solution was washed out of the microchannel with deionized (DI) water. The top-view optical microscopy image of the photopatterned posts showed homogeneous CaCO_3 /polymer composite microstructures with sharp edges (Figure 1b). In contrast, other procedures produced aggregated CaCO_3 seeds

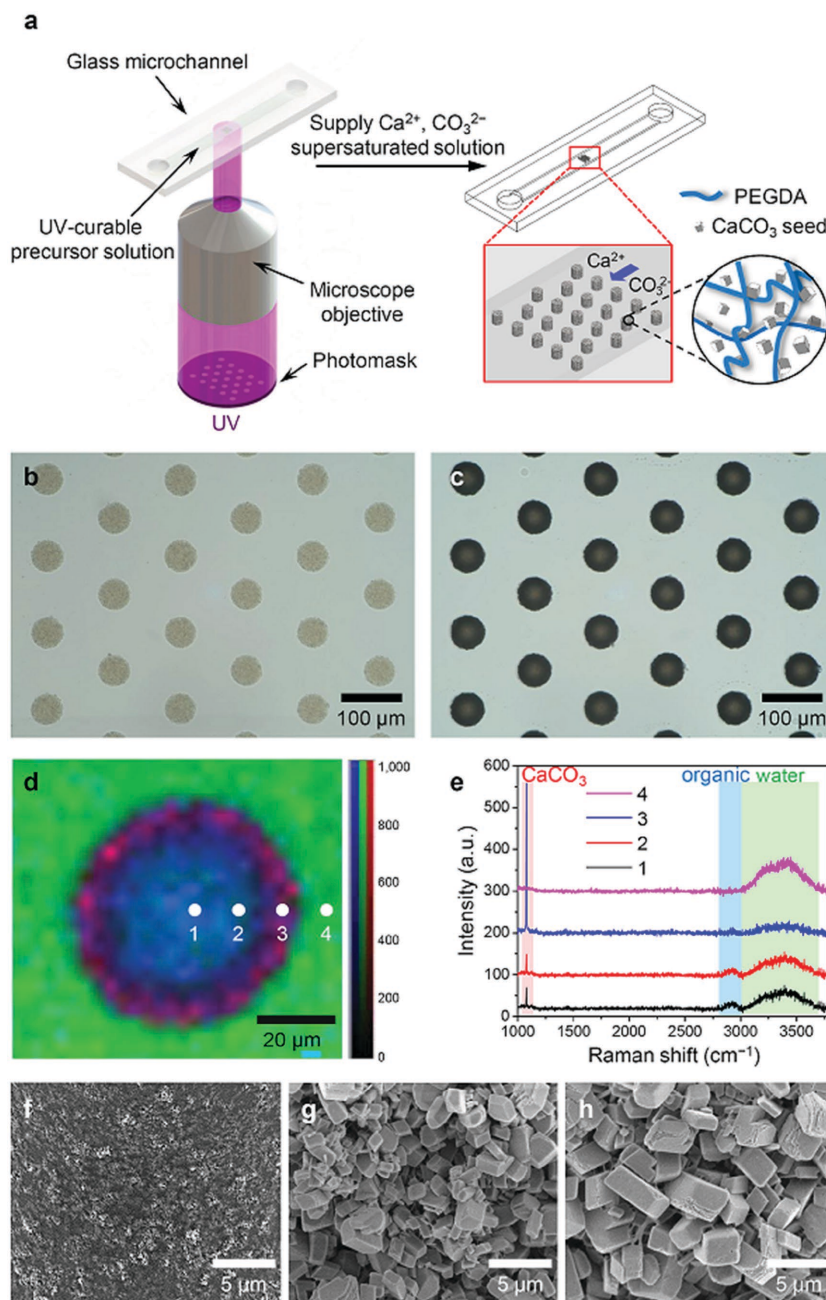


Figure 1. Design of mimicking rock micromodels. a) Schematic illustration showing the photolithographic patterning and the subsequent in situ growth of the CaCO_3 . b, c) Top-view optical microscopy images of CaCO_3 /polymer composite microstructures before b) and after c) growth of the CaCO_3 with supplying Ca^{2+} , CO_3^{2-} ions rich/supersaturated solutions. d, e) Raman mapping d) and spectrum e) of the composite post of (c) with different positions (1–4) obtained by integrating over the wavenumber ranges of CaCO_3 ($1050\text{--}1150\text{ cm}^{-1}$, red), organic ($2800\text{--}3000\text{ cm}^{-1}$, blue), and water ($3000\text{--}3700\text{ cm}^{-1}$, green), respectively. Mapping data were normalized to the strongest intensity of the CaCO_3 . At the position of 3, the intensity of CaCO_3 was maximized and the intensities of others were reduced by the growth of CaCO_3 . f–h) SEM images of the outer side surface of the composite posts with different growth time; (f), (g), and (h) indicate 0, 1, and 2 h, respectively.

in the precursor solutions, resulting in diffuse edge features and larger diameter of the post due to light scattering during UV-polymerization (Figure S1, Supporting Information).

The selective CaCO_3 growth on the posts is based on the biological strategy using Ca^{2+} , CO_3^{2-} ions in a supersaturated solution. A key advance in extending this CaCO_3 growth technique to create high quality CaCO_3 micromodels is the sustenance of the solution stability by supplying fresh solutions with fixed ionic composition ratios and frequent replacement, providing uniform CaCO_3 growth only in and on the posts. Spontaneous precipitation occurs when solutions are not replaced frequently, which leads to unwanted precipitation of CaCO_3 on the microchannel wall (Figure S1, Supporting Information). The stability of the supersaturated solution was confirmed by measuring pH (Figure S2, Supporting Information). These results indicate that the fast and selective growth of CaCO_3 required providing well-controlled supersaturated solutions.

Figure 1c shows the top-view optical microscopy image of CaCO_3 /polymer composite microstructures after CaCO_3 growth by using the optimized supersaturated solution for 1 h. Changes in the color and size of each post indicate the both inner and outer growth of CaCO_3 . In addition, the composite post shows axisymmetric shell structures as found by spatial scans with confocal Raman spectroscopic imaging (Figure 1d,e) revealing the distribution of CaCO_3 , organic, and water. The intensity of CaCO_3 is higher at the edge than in the inner parts of the posts, irrespective of z-section planes, which is consistent with the selective growth of CaCO_3 on the composite posts (Figure S3, Supporting Information). Scanning electron microscopy (SEM) images show the growth of the CaCO_3 seed particles on the post surface (Figure 1f–h and Figure S4, Supporting Information). The initial CaCO_3 particles were locally exposed at the surface of the composite posts, but after growth for 1 h, the post surfaces were fully covered with CaCO_3 particles. As the growth time increases, the size of the particles increases, which results in the increase in the diameter of the composite post. Crystals grown in our conditions have well-defined facets and smooth surface features, displaying equilibrium polyhedral (rhombohedral) morphologies. Also, the polymorph of CaCO_3 was confirmed as calcite by X-ray diffraction patterns and a Raman spectrum (Figures S5 and S6, Supporting Information). No characteristic peak from other phases of CaCO_3 is found, suggesting that the CaCO_3 is totally composed of calcite crystals throughout the growth period.

2.2. CaCO_3 Growth

In addition to photopatterning, controlling the CaCO_3 growth of the composite microposts is important to tune the geometry of micromodels. To quantify the growth rate of the CaCO_3 , we investigated the change in the dimension of two different sizes of single microposts as a function of the growth time using the optimized supersaturated solution. Inverse monochrome optical microscopy images from top view of the posts are shown in Figure 2a, where bright areas of the optical microscopy images indicate in situ grown CaCO_3 . Figure 2b shows the variation of the intensity with the radial distance where one can observe that there is inward as well as outward growth of the CaCO_3 /polymer composite posts. We recognized that there is a mechanistic difference between the inward and the outward growth since though the distance between the initial post radius (R_0) and the inner radius (R_{in}) of dark part ($R_0 - R_{\text{in}}$)

becomes constant very quickly, outer post radius (R_{out}) varies linearly with time (Figure 2c).

The outward growth of CaCO_3 happens through the precipitation of fresh ions on the outer layer of the post. Therefore, the outward growth can be approximated as a surface reaction. Since convection, diffusion and reaction occur simultaneously in this process, it is important to understand the relative importance of these phenomena. For the sake of simplicity, we assumed that mass transfer coefficient is infinity or the concentration of ions on the post surface is the same as the fresh ion concentration, i.e., $[\text{Ca}^{2+}]_0$ and $[\text{CO}_3^{2-}]_0$ (we relaxed this assumption during our next discussion). With this assumption, we were able to predict the mass balance equation

$$\frac{dR_{\text{out}}}{dt} = \frac{k''([\text{Ca}^{2+}]_0[\text{CO}_3^{2-}]_0 - K_{\text{SP}}/f_D^2)}{\rho_{\text{CaCO}_3}} \quad (1)$$

where k'' is the surface reaction rate constant, ρ_{CaCO_3} is the molar density of CaCO_3 , K_{SP} is its solubility product constant, and f_D is the activity coefficient for divalent ions. This relationship predicts the growth rate of R_{out} for CaCO_3 as a function of $[\text{Ca}^{2+}]_0$ and $[\text{CO}_3^{2-}]_0$ concentrations and allows us to quantitatively determine how the performance of the system depends on the supersaturated solutions. Upon substituting the known values of $k'' = 2.32 \times 10^{-4} \text{ m}^4 \text{ mol}^{-1} \text{ s}^{-1}$, $[\text{Ca}^{2+}] = 0.57 \times 10^{-3} \text{ M}$, $[\text{CO}_3^{2-}] = 0.33 \times 10^{-3} \text{ M}$, $\rho_{\text{CaCO}_3} = 27.1 \text{ mol L}^{-1}$, $K_{\text{SP}} = 3.14 \times 10^{-9} \text{ M}^2$ and $f_D = 0.561$ (see the Supporting Information for details), we obtain a theoretically predicted growth rate of $5.5 \mu\text{m h}^{-1}$. The predicted rate is very close to the experimentally observed value of $4.8 \mu\text{m h}^{-1}$. Also, experiments are consistent with the prediction of Equation (1) that growth rate remains the same regardless of post size (Figure 2c).

Unlike the outward growth, the mechanism of the inward growth of CaCO_3 can be quantitatively predicted by relating the reaction time scale to the diffusion time scale. Since the crystal seeds are distributed uniformly inside the posts, inward growth of CaCO_3 can be approximated as a volumetric reaction. Hence, we can define Damköhler number as

$$Da = \frac{k'''[\text{Ca}^{2+}]_0 R_0^2}{D_{\text{ion,post}}} \quad (2)$$

where k''' is the volumetric rate constant, $[\text{Ca}^{2+}]_0$ is the concentration of fresh calcium ions, and $D_{\text{ion,post}}$ is the diffusivity of ions inside the post. The values of k''' is $3.66 \times 10^5 \text{ L mol}^{-1} \text{ s}^{-1}$ (see the Supporting Information for details) and we assumed that diffusivity of ions in the post will be on the same order of magnitude as diffusivity of ions inside aqueous medium or $D_{\text{ion,post}} \approx 10^{-9} \text{ m}^2 \text{ s}^{-1}$. Upon substituting the values of $k''' = 3.66 \times 10^5 \text{ L mol}^{-1} \text{ s}^{-1}$, $D_{\text{ion,post}} = 10^{-9} \text{ m}^2 \text{ s}^{-1}$, $[\text{Ca}^{2+}] = 0.57 \times 10^{-3} \text{ M}$, $R_0 = 25$ or $50 \mu\text{m}$, we find that $Da \gg 1$ for both the small and large posts. Hence, reaction will dominate the process and ions will be present only in the boundary layer region with thickness given by $\delta \approx R_0/\sqrt{Da}$ or

$$\delta \approx \sqrt{D_{\text{ion,post}}/k'''[\text{Ca}^{2+}]_0} \quad (3)$$

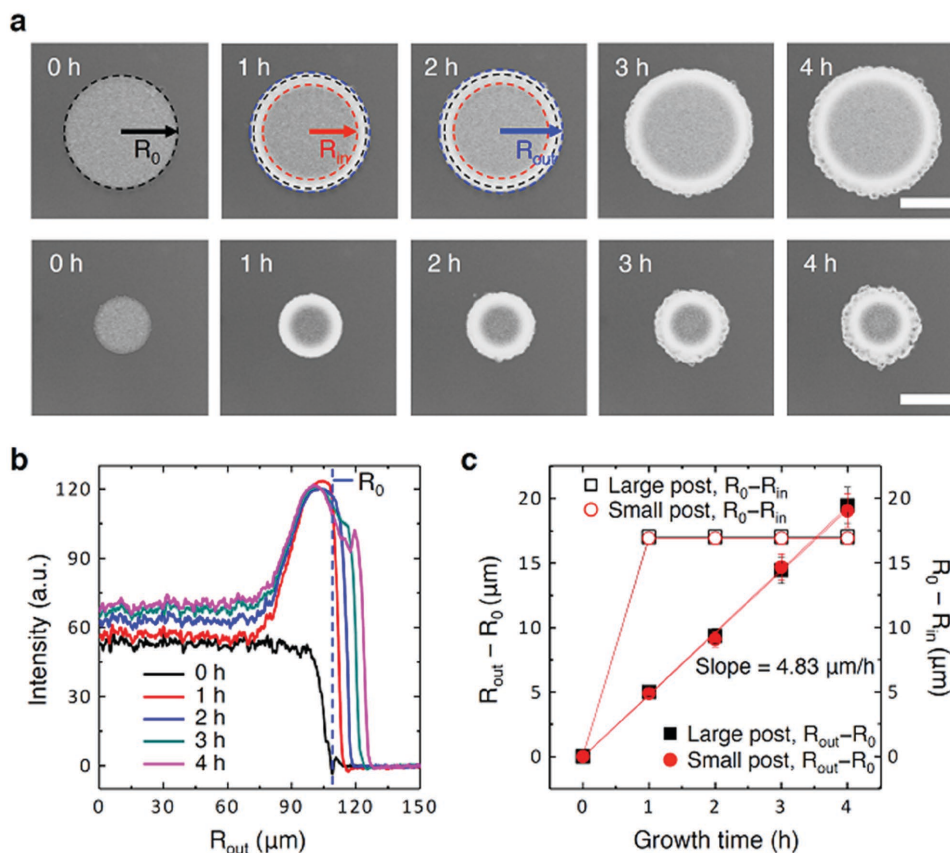


Figure 2. In situ growth of CaCO_3 posts. a) In situ optical microscopy images of CaCO_3 /polymer composite posts in the channel versus growth time. R_0 , R_{in} , and R_{out} indicate the initial radius, the inner radius of the dark part, and the outer radius of the posts, respectively. All the scale bars are $100 \mu\text{m}$. b) Gray intensity profiles (a.u. = arbitrary units) taken across centered regions of the large post with the different growth time. The blue dashed line indicates R_0 . c) The changes in $R_{out} - R_0$ (black solid square: large post, red solid circle: small post) and $R_0 - R_{in}$ (black open square: large post, red open circle: small post) as a function of the growth time.

This simple expression predicts $\delta \approx 2.2 \mu\text{m}$, which is on the same order of magnitude as the experimentally observed value of $R_0 - R_{in}$ of $17 \mu\text{m}$. Further, since the system is diffusion limited, the boundary layer thickness would be the same irrespective of the post size. This is also reflected in Equation (3) and also observed experimentally (Figure 2c). Finally, the time scale for the boundary layer to develop is given by the diffusion time scale $t_D \approx R_0^2 / D_{ion,post}$. Upon substitution, t_D is 10 s for large posts. Even if the post size is as long as the channel width (1 mm), t_D is no more than 5 min. Hence, we did not see a change in $R_0 - R_{in}$ as a function of time in Figure 2c.

We investigated the effect of $R_0 - R_{in}$ and the rate of change in $R_{out} - R_0$ with the concentration of supersaturated solutions related to the reaction rate (Figure S7, Supporting Information). When we reduced the concentration of both CaCl_2 and NaHCO_3 solutions by half to 0.8×10^{-3} and $20 \times 10^{-3} \text{ M}$, $R_0 - R_{in}$ increased to 25 from $17 \mu\text{m}$. This change occurs because when the ionic concentration is reduced to half, the boundary layer thickness increases by a factor of $\sqrt{2}$ (Equation (3)). Also, the rate of change in $R_{out} - R_0$ decreased fourfold to 1.2 from $4.8 \mu\text{m h}^{-1}$, as predicted by Equation (1). Hence, we demonstrate an ability to predict and control the inward and outward growth rates of CaCO_3 in a single post.

2.3. Micromodel Geometry

Controlling geometries to submicrometer pore-length scales, particularly those with photolithography and etching, has proved difficult by using conventional methods for micromodels.^[4] Tuning porosity and permeability, which are sensitive to changes in micromodel geometry, notoriously requires restructuring of intricate topographical elements that are hard to change. Polymeric micromodels show more promise in terms of restructuring geometry by using additional lithographic process, notably, but they still fail with the control of submicrometer scales.^[14] In our CaCO_3 /polymer composite system, the photopatternable microposts serves as an artificial support that allows CaCO_3 to grow, and the growth of CaCO_3 enables the pores of the micromodel to be tuned *dynamically*, down to submicrometer gap widths between the posts. **Figure 3a** demonstrates this ability for heterogeneous structures composed of two kinds of square posts arranged in a rectangular array with different dimensions in a single microchannel. The CaCO_3 grows rapidly on both posts for initial 4 h period, after that, it grows more slowly, and in the latter state comes into direct contact with the CaCO_3 of neighboring small posts in the vertical position. The minimum gap widths between the small posts in the 3rd and 4th rows near the channel wall reduced from

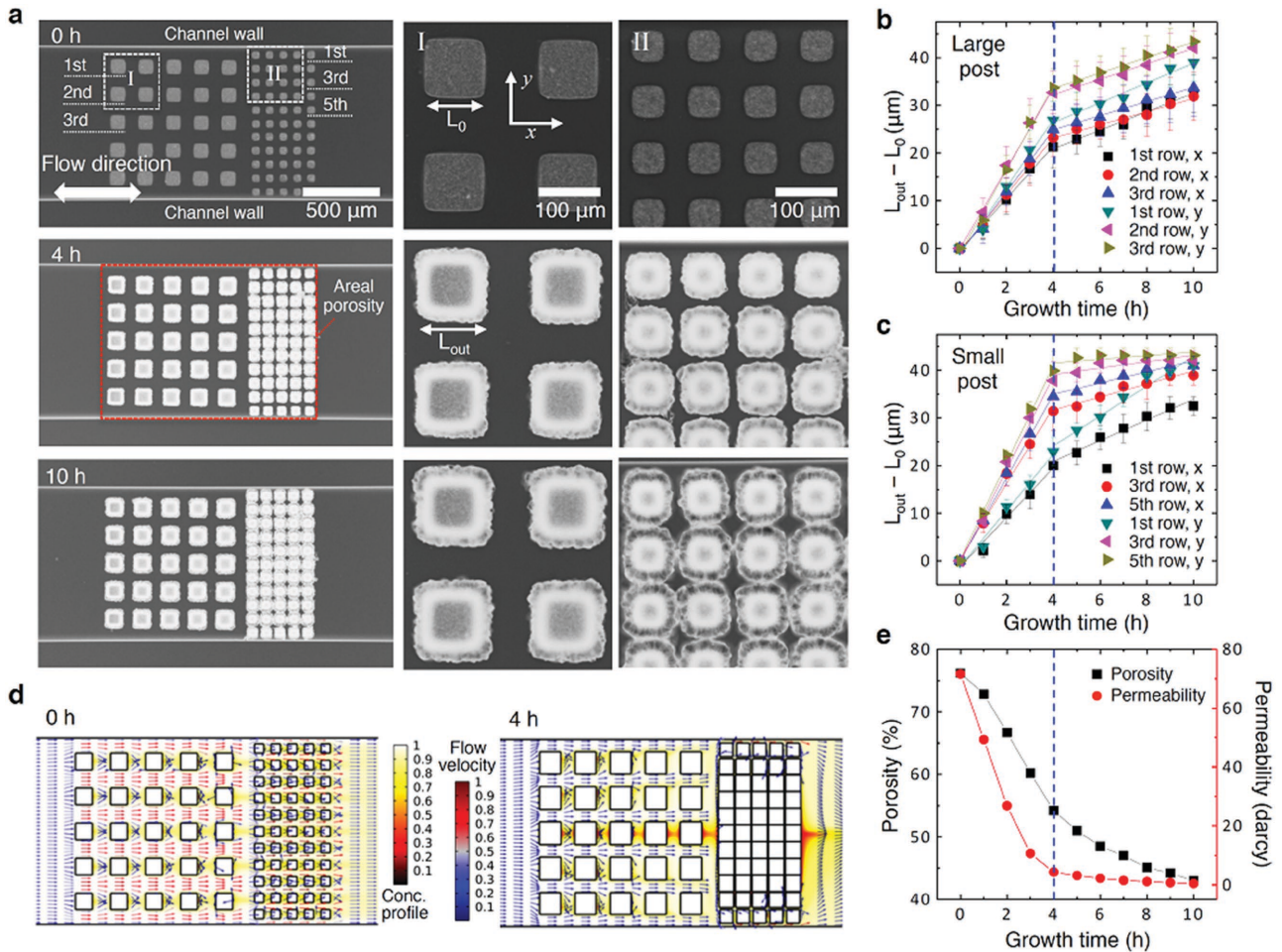


Figure 3. Growth of CaCO₃ posts with heterogeneous structures. a) Optical microscopy images of the heterogeneous CaCO₃ posts (side lengths, 100 and 50 μm) with different growth time (0, 4, and 10 h) using the supersaturated solution. The right images are magnified views of the white dotted boxes in the left images. The red dotted box indicates the area for the calculation of a void fraction (porosity). L_0 and L_{out} indicate the initial length and the outer length of the posts, respectively. b, c) $L_{out} - L_0$ versus growth time of the large b) and small c) posts with different positions and directions. The blue dashed lines indicate the transition to slow CaCO₃ growth. d) Simulation results of the dimensionless concentration $[Ca^{2+}]/[Ca^{2+}]_0$ (background colors) and dimensionless flow velocity u/u_{max} (arrow colors) of the supersaturated solution throughout the multiposts with different growth time (0 and 4 h). e) Measured areal porosity of the red dotted area in (a) and computed permeability (1 darcy = 0.987 μm²) of the same region as a function of the growth time (see Figure S5, Supporting Information, for details).

40 μm (0 h) to 2 μm (4 h), and to less than 1 μm (at 10 h the gap is not resolvable in our setup), presumably resulting in the nanochannels formed by merging some parts of two CaCO₃ posts. These posts have position-dependent growth of CaCO₃ as a result of different boundary layer thickness around different posts. Figure 3b,c shows the changes in dimensions of each post with side lengths of 100 μm (large) and 50 μm (small), respectively, near and far from the channel wall as a function of growth time. As one observes from the experimental results, the behavior of CaCO₃ growth is quite different before and after 4 h (Table S4, Supporting Information).

First, we focus on growth behavior before 4 h. The growth rate of CaCO₃ on the post side in parallel (y -direction) with the flow direction is faster than that perpendicular to the flow direction (x -direction). Furthermore, we detected the growth rate of the posts in the 1st row near the channel wall is the slowest in both large and small posts, consistent with the

slower tendency of x -direction growth than y -direction. Finally, the growth rate of smaller posts is faster than larger posts, an effect not observed in the case of single posts. To develop an understanding of these results, we developed a COMSOL model where we solved the momentum equation coupled with species transport equation (see the Supporting Information for details). The obtained results suggested that the dimensionless concentration $[Ca^{2+}]/[Ca^{2+}]_0$ is higher in the regions of higher dimensionless velocity u/u_{max} (Figure 3d at 0 h). This is expected since the mass transfer coefficient will be higher in the regions of higher velocity and the concentration would be closer to the fresh ionic concentration. Since the velocity is higher in the region of vertical gaps between the posts, the growth rate in y -direction is higher than the growth rate in x -direction. Moreover, because of higher velocities in the vertical gaps between smaller posts as compared to larger posts, the growth rate is higher for smaller posts. This effect is not

observed for single posts since the velocity (and mass transfer coefficient) is practically independent of post size. Finally, the effect of slower growth rate of posts near the walls is not captured in our simulations. We believe that this happens because our simulations assume a very homogenous spatial distribution of posts whereas in experiments there is some heterogeneity in the spatial distribution.

At 4 h, the gap between small posts in the center of the channel reduces to a few micrometers. Thus we observe a reduction in flow rate to about 20% of the initial value (estimated through the COMSOL model) and a slower CaCO_3 growth for all posts (the blue dashed lines in Figure 3b,c demarcate the onset of the slow growth period). Also, a higher flow resistance in the central part of the channel forces the flow to go through the region near walls (Figure 3d at 4 h) and hence, after 4 h the growth rate is highest in the 1st row (Figure 3b,c). These results show that the local differences in the flow velocity induced by geometry affect the regional growth of CaCO_3 .

Two parameters that are often used to characterize porous media are porosity and permeability. Changes in the areal porosity with the growth time were calculated from the optical microscopy images of CaCO_3 posts (Figure 3e and see Figure S8, Supporting Information, for details). The porosity decreases continuously from 76% to 43% over the period of 10 h. There is spatial heterogeneity in local porosity due to the different post sizes (Figure 3a). Our method allows us to create structures with a wide range of porosities simply by changing the lithographic mask and hence post size. Further, the method provides a simple way to control the porosity of a micromodel in time by varying the flow of the supersaturated solutions.

Due to well-known experimental challenges in measuring small flow rates in microfluidic channels,^[53] we estimated the permeability in the region around posts (same area in which the areal porosity was measured) using a COMSOL model (see Figure 3e, Supporting Information, for details). There is a rapid decrease in permeability in the first 4 h from 72 to 4 darcy due to high CaCO_3 growth in the central region of the channel. After 4 h, almost the entire pressure drop in the channel is concentrated across the post region. A tenfold reduction in the flow rate is observed from 4 to 10 h due to continuous increase in the flow resistance associated with CaCO_3 growth. After 10 h, the permeability is estimated to be 0.4 darcy. The permeabilities we obtain during 4–10 h are within the reported permeability range for Arab-D reservoirs.^[54]

2.4. Acid Fracturing

In the petroleum industry, acid injection is used to enhance the reservoir permeability during secondary and tertiary recovery. In spite of the importance of this practice, core-based methods and conventional micromodels have not been able to demonstrate the geochemical fluid–rock interaction due to their opaqueness or other material limitations. Carbonate micromodels are the only micromodels that can be used to understand the acid fracturing process.^[20] Using our micromodel, flow-induced dissolution was observed and imaged over time as acidic brine flooded through the channel (Figure 4). Figure 4a shows the early-stage dissolution process of the heterogeneous micromodels over a

period of 2 min. CO_2 bubbles were first observed around the large CaCO_3 post array, and then the small post array, as acidic brine flowed from left to right. The acidic brine flowed through the bottom section of the small post array (red dotted box in Figure 4a), because this section had the lowest flow resistance. As a result, the dissolution of CaCO_3 posts propagated from the left wall to the right wall of the channel in the small post area (Figure 4b). From this phenomenon, it can be inferred that flow and dissolution are correlated with each other.^[20] Figure 4c, a graph representing the CaCO_3 fraction change in the fixed area over time, shows an exponential decay trend. This trend can be attributed to the initial fast decrease in the large post array, followed by the approximately linear decrease in the small post array (about 2.5 rows of posts every 4 min). To our knowledge, this study is the first demonstration of both CaCO_3 formation and dissolution in a single micromodel. We conducted an additional acid fracturing experiment using another CaCO_3 micromodel and the images are available in Figure S10 (Supporting Information).

2.5. Large-Area Fabrication

An additional advantage of our route to produce synthetic micromodels is the large-area fabrication of multiple CaCO_3 posts in a microchannel. Compared to the conventional microscope-based lithography (Figure 1a), a customized contact lithography system generates strong and homogeneous illumination and thus allows a wide effective area maintaining excellent resolution.^[55] Figure 5a shows the CaCO_3 micromodels fabricated by the contact lithography with a specially designed chrome photomask (Figure S11, Supporting Information). The size and overall shape of polymerized structures are in excellent agreement with the mask pattern, with sharp edges. The posts become dark and large as the growth time increases for 2 h. The round-shaped posts arranged in zigzag array also enable the regional growth to be more homogeneous than the square posts arranged in a rectangular array, which may be attributed to a decrease in the local difference of the flow velocity induced by geometry (Figure S12, Supporting Information). To ensure that we have uniform supply of Ca^{2+} and CO_3^{2-} ions for all the posts in the large-area fabrication experiments, we injected the supersaturated solution into the channel from opposite directions every 30 min at a high flow rate (see the calculation on mass balance of ions in the Supporting Information).

2.6. Wettability

In addition to geometry and porosity, tuning wettability of CaCO_3 micromodels makes it possible to understand fundamental fluid behavior and interactions among oil–water–rock phases. Although the CaCO_3 inherently shows water-wet behavior in the presence of oil and water (Figure S13a, Supporting Information), the surface wettability of CaCO_3 reservoirs is known to be mostly (84%) oil-wet.^[56] Our CaCO_3 micromodel can be treated by stearic acid to decrease the surface energy of CaCO_3 ^[57] (Figure S13b, Supporting

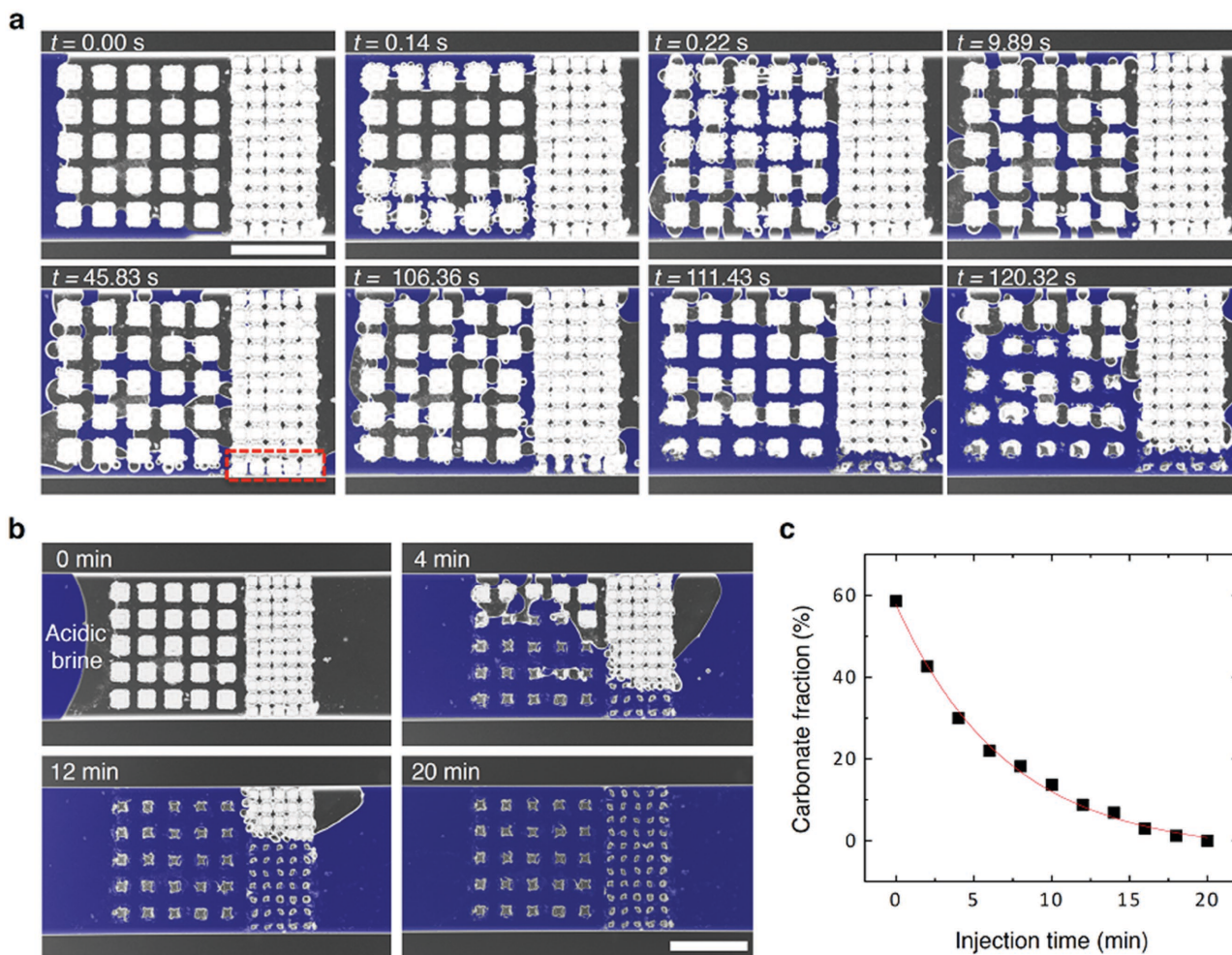


Figure 4. Acid fracturing of the heterogeneous CaCO_3 micromodel. a,b) The sequential optical microscopy images showing the dissolution process of the CaCO_3 micromodel under acidic brine (1% HCl, 1.81 M NaCl in deionized water) injection (flow direction from left to right) (scale bar, 500 μm). The blue color highlights the region of the acidic brine. Original images are in Figure S9 (Supporting Information). The red dotted box indicates the lowest flow resistance region in the small post array. c) Areal fraction of CaCO_3 in the micromodel versus the injection time of the acidic brine. The area for the calculation of a CaCO_3 fraction is the same as Figure 3e.

Information). Immiscible fluids were sequentially injected into the untreated CaCO_3 micromodel at constant pressures (water \rightarrow decane \rightarrow water). All of the water-wet posts were encapsulated by water (Figure 5b and Figure S14a, Supporting Information). After water was reintroduced to the channel, decane in the channel was entirely washed away (Figure 5c). In the opposite flow sequence (decane \rightarrow water \rightarrow decane), the oil-wet posts treated by stearic acid left decane at the posterior area (Figure 5d and Figure S14b, Supporting Information). After decane was reintroduced to the channel, water was replaced by decane, but water near side walls was left regionally due to the water-wet surface of the acrylate-functionalized channel walls (Figure 5e). These results show water-wet and oil-wet posts always had the same result of totally wetting with respect to their preferred phases. With further experiments using CaCO_3 micromodels, we can broaden our understanding of how the geochemical properties of a micromodel are correlated to and affect the displacement process for EOR.

3. Conclusion

Our CaCO_3 micromodel provides new capabilities for the design of mimicking rock microfluidic systems with dynamically tunable geometry, porosity, and wettability. By pairing photolithographic technique with site-selective mineralization, we can mimic real carbonate reservoir properties that encompass heterogeneous geometries containing a wide range of length scales, porosities, and permeabilities. Specifically, by flowing Ca^{2+} , CO_3^{2-} ions rich/supersaturated solution we controlled CaCO_3 growth to dynamically adjust the structure's geometry. This allowed us to achieve small flow channels between the posts, falling within the length scales characteristic of microporous reservoirs ($< 10 \mu\text{m}$ pores). Once the initial CaCO_3 structures have been created, their surface geochemistry can be altered by flowing fluids such as oil, water, CO_2 and acids, as demonstrated in the acid fracture experiment. The ability to tune the wettability of CaCO_3 and directly observe complex multiphase flows and geochemical fluid- CaCO_3 interactions,

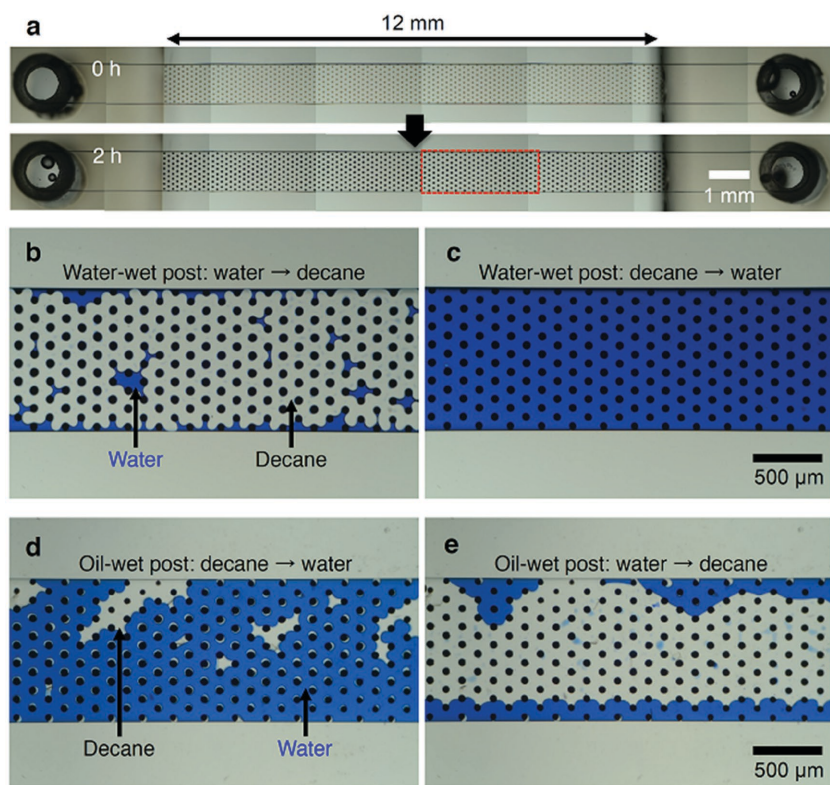


Figure 5. Multipost array oil–water displacement experiments. a) Optical microscopy images of the CaCO_3 posts fabricated by a contact lithography. The posts were gradually grown through supplying the supersaturated solution from 0 to 2 h. The red dotted box indicates the area of (b–e). b,c) With this micromodel, water → decane → water flow experiment was conducted (flow direction from left to right). When decane displaced water (colored with methylene blue), water was selectively left in the water-wet posts b). After water was reintroduced to the channel, decane in the channel was entirely washed away c). d,e) The micromodel was treated by a stearic acid. Thereafter, decane → water → decane flow experiment was conducted. When water displaced water, oil-wet posts held decane d). After decane was reintroduced to the channel, water was replaced by decane, but water near side walls was left regionally e).

makes this technique a very useful platform for studies in water flooding, CO_2 storage, CO_2 -EOR, and chemical EOR.^[58,59]

The in situ grown CaCO_3 micromodels can be utilized for other applications in mineralogy, geology, and reservoir engineering. In our system, amorphous and metastable crystalline CaCO_3 can be used as seed nanoparticles to study the transformation mechanism of CaCO_3 polymorphs. Further, their transformation and stabilization can be controlled by various reaction parameters.^[60–62] The approach can be extended to prepare magnesium (Mg)-bearing carbonate by using different anhydrous supersaturated Ca–Mg– CO_3 solutions,^[63] thereby facilitating the preparation of different types of synthetic carbonate reservoir micromodels. Our method also allows for precise control of mass transfer and can serve as a good model system to investigate crystal growth. Combining the micromodel with in situ spectroscopic imaging techniques, such as Raman or fluorescence, one can monitor the changes in polymorphs and morphologies which will reveal mechanisms of coprecipitation processes.^[64–66] Advanced in situ spectroscopic techniques can also be used to visualize adsorption or desorption of chemical species on the carbonate rocks. Hence, this method can provide better understanding of chemical and physical features at

oil/rock or water/rock interfaces as well as screening chemicals for EOR.

4. Experimental Section

Fabrication of CaCO_3 Micromodels: A glass microfluidic channel (Hilgenberg GmbH, Germany) was filled with 1 M sodium hydroxide aqueous solution for 1 h, followed by rinsing with DI water. After filling the microchannel with 3-(trimethoxysilyl)propyl acrylate (Sigma-Aldrich) for 5 min, the channel was thoroughly rinsed with ethanol and DI water. The channel was cured at 80 °C for 30 min. The precursor solution was prepared by dissolving 5 mg CaCO_3 nanoparticles (Solvay chemicals, calcite, 50–100 nm in diameter) in the 100 μL solution containing 20 μL of poly(ethylene glycol) diacrylate (Sigma-Aldrich, $M_n \approx 700$), 5 μL of 2-hydroxy-2-methylpropiofenone (Darocur, Sigma-Aldrich), 40 μL of poly(ethylene glycol) (Sigma-Aldrich, $M_w \approx 200$), and 35 μL of DI water. Ultrasonicator (Cole-Parmer) was used to disperse the CaCO_3 particles into the solution. The well-dispersed precursor solutions were injected into the acrylate-functionalized microchannel, followed by UV photolithography using the photomask inserted into the field stop of the inverted microscope (Zeiss Axio Observer A1)^[14] or customized contact photolithography instruments.^[55] UV exposure was controlled by switching a light-emitting diode (LED) light source on and off with LabView. After building microstructured posts, any uncured precursor solution was washed out of the microchannel with DI water. Ca^{2+} , CO_3^{2-} ions rich/supersaturated solutions were prepared by the dropwise addition of 100 mL of sodium bicarbonate solution (40×10^{-3} M) to 100 mL of calcium chloride solution (1.6×10^{-3} M). The solutions were injected into the as-prepared microchannel with the constant inlet pressure and alternate directions, which were replaced fresh ones every 30 min. The reaction was achieved under relatively high (40 °C) temperature, which was chosen based on experimental optimization. The CaCO_3 was treated by the ethanol solution of stearic acid (4.0 wt%) for 60 min, followed by rinsing with ethanol and drying. The sample dissolution experiment was performed using acidic brine (1% hydrochloric acid, 1.81 M sodium chloride in DI water) under constant flow rate (0.5 mL min^{-1}). For oil–water displacement experiments, two immiscible fluids were serially introduced into the channel under constant flow rate (0.1 mL min^{-1}).

Sample Characterization: The micromodels were imaged by optical microscopy (Zeiss Axio Observer A1), confocal Raman microscopy (Horiba LabRam HR), and SEM (JEOL-6010LA). X-ray analysis was performed using a PANalytical X'Pert PRO X-ray powder diffractometer (XRPD). For confocal Raman microspectroscopy, the selected area of the sample was scanned with a continuous green laser beam with lateral and depth resolutions of 250 and 500 nm, respectively. Raman images have been generated by integrating the intensity of the signal for the wavenumber ranges of CaCO_3 ($1050\text{--}1150 \text{ cm}^{-1}$), organic ($2800\text{--}3000 \text{ cm}^{-1}$), and water ($3000\text{--}3700 \text{ cm}^{-1}$). For SEM and XRPD, samples were prepared on poly(dimethyl siloxane) (PDMS) microfluidic channels, followed by delaminating PDMS from the glass. Critical point dryer was used for the sample of SEM. The post dimensions and areal porosity of the samples were measured by ImageJ and optical microscopy images with time. The water contact angles on the sample were measured in a quartz cell filled with decane using a goniometer (Rame-Hart). The pH changes

accompanying CaCO₃ precipitation were followed using a pH meter (Thermo Scientific) at 20 °C.

Simulation: COMSOL Multiphysics 5.1 was used to perform simulations. Momentum equation and species transport equations were solved simultaneously to obtain a steady state solution.

Supporting Information

Supporting Information is available from the Wiley Online Library or from the author.

Acknowledgements

This research was supported by the National Science Foundation (NSF) grant CMMI-1120724. H.L. acknowledges partial support from a Samsung Fellowship. Raman measurement and 3D Raman mapping were conducted at Aramco Services Company: Aramco Research Center—Boston using confocal Raman microscope system. We acknowledge Dr. Wei Wang (Aramco Services Company) for helpful discussions about Raman mapping.

Received: February 1, 2016

Revised: March 25, 2016

Published online:

- [1] C. U. Hatiboglu, T. Babadagli, *Phys. Rev. E* **2008**, *77*, 066311.
- [2] C. Cottin, H. Bodiguel, A. Colin, *Phys. Rev. E* **2011**, *84*, 026311.
- [3] C. Zhang, M. Oostrom, T. W. Wietsma, J. W. Grate, M. G. Warner, *Energy Fuels* **2011**, *25*, 3493.
- [4] N. K. Karadimitriou, S. M. Hassanizadeh, *Vadose Zone J.* **2012**, *11*.
- [5] J. Joseph, N. S. K. Gunda, S. K. Mitra, *Chem. Eng. Sci.* **2013**, *99*, 274.
- [6] D. Sinton, *Lab Chip* **2014**, *14*, 3127.
- [7] J. W. Grate, R. T. Kelly, J. Suter, N. C. Anheier, *Lab Chip* **2012**, *12*, 4796.
- [8] N. K. Karadimitriou, V. Joekar-Niasar, S. M. Hassanizadeh, P. J. Kleingeld, L. J. Pyrak-Nolte, *Lab Chip* **2012**, *12*, 3413.
- [9] N. S. K. Gunda, B. Bera, N. K. Karadimitriou, S. K. Mitra, S. M. Hassanizadeh, *Lab Chip* **2011**, *11*, 3785.
- [10] V. Berejnov, N. Djilali, D. Sinton, *Lab Chip* **2008**, *8*, 689.
- [11] E. Sollier, C. Murray, P. Maoddi, D. Di Carlo, *Lab Chip* **2011**, *11*, 3752.
- [12] K. W. Bong, J. Xu, J.-H. Kim, S. C. Chapin, M. S. Strano, K. K. Gleason, P. S. Doyle, *Nat. Commun.* **2012**, *3*, 805.
- [13] M. Wu, F. Xiao, R. M. Johnson-Paben, S. T. Retterer, X. Yin, K. B. Neeves, *Lab Chip* **2012**, *12*, 253.
- [14] H. Lee, S. G. Lee, P. S. Doyle, *Lab Chip* **2015**, *15*, 3047.
- [15] C.-Y. Wu, K. Owsley, D. Di Carlo, *Adv. Mater.* **2015**, *27*, 7970.
- [16] M. H. Schneider, H. Willaime, Y. Tran, F. Rezgui, P. Tabeling, *Anal. Chem.* **2010**, *82*, 8848.
- [17] B. Levache, A. Azioune, M. Bourrel, V. Studer, D. Bartolo, *Lab Chip* **2012**, *12*, 3028.
- [18] K. Ma, R. Lontas, C. A. Conn, G. J. Hirasaki, S. L. Biswal, *Soft Matter* **2012**, *8*, 10669.
- [19] J. W. Grate, M. G. Warner, J. W. Pittman, K. J. Dehoff, T. W. Wietsma, C. Zhang, M. Oostrom, *Water Resour. Res.* **2013**, *49*, 4724.
- [20] W. Song, T. W. de Haas, H. Fadaei, D. Sinton, *Lab Chip* **2014**, *14*, 4382.
- [21] M. L. Porter, J. Jimenez-Martinez, R. Martinez, Q. McCulloch, J. W. Carey, H. S. Viswanathan, *Lab Chip* **2015**, *15*, 4044.
- [22] K. M. Bartko, H. A. Nasr-El-Din, Z. Rahim, G. A. Al-Muntasheri, in *SPE Annual Technical Conference and Exhibition*, Society of Petroleum Engineers, Denver, Colorado, October **2003**.
- [23] S. Davies, S. Kelkar, *Middle East Asia Reservoir Rev.* **2007**, *8*, 51.
- [24] D. L. Cantrell, R. M. Hagerty, *GeoArabia* **1999**, *4*, 129.
- [25] T. M. Okasha, J. J. Funk, H. N. Rashidi, in *SPE Middle East Oil and Gas Show and Conference*, Society of Petroleum Engineers, Manama, Bahrain, March, **2007**.
- [26] A. Heuer, D. Fink, V. Laraia, J. Arias, P. Calvert, K. Kendall, G. Messing, J. Blackwell, P. Rieke, D. Thompson, A. Wheeler, A. Veis, A. Caplan, *Science* **1992**, *255*, 1098.
- [27] L. B. Gower, *Chem. Rev.* **2008**, *108*, 4551.
- [28] S. Weiner, L. Addadi, in *Annual Review of Materials Research* (Eds: D. R. Clarke, P. Fratzl), Vol. 41, Annual Reviews, Palo Alto, **2011**, p. 21.
- [29] E. Asenath-Smith, H. Li, E. C. Keene, Z. W. Seh, L. A. Estroff, *Adv. Funct. Mater.* **2012**, *22*, 2891.
- [30] G. Falini, S. Albeck, S. Weiner, L. Addadi, *Science* **1996**, *271*, 67.
- [31] J. Aizenberg, A. J. Black, G. M. Whitesides, *Nature* **1999**, *398*, 495.
- [32] J. Aizenberg, D. A. Muller, J. L. Grazul, D. Hamann, *Science* **2003**, *299*, 1205.
- [33] X. Xu, J. T. Han, K. Cho, *Chem. Mater.* **2004**, *16*, 1740.
- [34] J. T. Han, X. Xu, D. H. Kim, K. Cho, *Adv. Funct. Mater.* **2005**, *15*, 475.
- [35] H. Li, H. L. Xin, D. A. Muller, L. A. Estroff, *Science* **2009**, *326*, 1244.
- [36] A. Finnemore, P. Cunha, T. Shean, S. Vignolini, S. Guldin, M. Oyen, U. Steiner, *Nat. Commun.* **2012**, *3*, 966.
- [37] F. Natalio, T. P. Corrales, M. Panthoefler, D. Schollmeyer, I. Lieberwirth, W. E. G. Mueller, M. Kappl, H.-J. Butt, W. Tremel, *Science* **2013**, *339*, 1298.
- [38] K. Lee, W. Wagermaier, A. Masic, K. P. Kommareddy, M. Bennet, I. Manjubala, S. W. Lee, S. B. Park, H. Colfen, P. Fratzl, *Nat. Commun.* **2012**, *3*, 725.
- [39] O. Grassmann, G. Müller, P. Löbmann, *Chem. Mater.* **2002**, *14*, 4530.
- [40] Y. Kitano, *Bull. Chem. Soc. Jpn.* **1962**, *35*, 1973.
- [41] W. L. Noorduin, A. Grinthal, L. Mahadevan, J. Aizenberg, *Science* **2013**, *340*, 832.
- [42] X. Gong, Y.-W. Wang, J. Ihli, Y.-Y. Kim, S. Li, R. Walshaw, L. Chen, F. C. Meldrum, *Adv. Mater.* **2015**, *27*, 7395.
- [43] S. Mann, G. A. Ozin, *Nature* **1996**, *382*, 313.
- [44] B. Kowalczyk, K. J. Bishop, I. Lagzi, D. Wang, Y. Wei, S. Han, B. A. Grzybowski, *Nat. Mater.* **2012**, *11*, 227.
- [45] A. M. Tartakovsky, G. Redden, P. C. Lichtner, T. D. Scheibe, P. Meakin, *Water Resour. Res.* **2008**, *44*, W06S04.
- [46] G. E. Katz, B. Berkowitz, A. Guadagnini, M. W. Saaltink, *J. Contam. Hydrol.* **2011**, *120–121*, 27.
- [47] R. Singh, H. Yoon, R. A. Sanford, L. E. Katz, B. W. Fouke, C. J. Werth, *Environ. Sci. Technol.* **2015**, *49*, 12094.
- [48] P. A. Raj, M. Johnsson, M. J. Levine, G. H. Nancollas, *J. Biol. Chem.* **1992**, *267*, 5968.
- [49] R. H. Clark, A. A. Campbell, L. A. Klumb, C. J. Long, P. S. Stayton, *Calcif. Tissue Int.* **1999**, *64*, 516.
- [50] M. Kawashita, M. Nakao, M. Minoda, H. M. Kim, T. Beppu, T. Miyamoto, T. Kokubo, T. Nakamura, *Biomaterials* **2003**, *24*, 2477.
- [51] H. Lee, R. L. Srinivas, A. Gupta, P. S. Doyle, *Angew. Chem. Int. Ed.* **2015**, *54*, 2477.
- [52] G. H. Nancollas, M. M. Reddy, *J. Colloid Interface Sci.* **1971**, *37*, 824.
- [53] D. J. Beebe, G. A. Mensing, G. M. Walker, *Annu. Rev. Biomed. Eng.* **2002**, *4*, 261.
- [54] A. S. Alsharhan, K. Magara, *Facies* **1995**, *32*, 237.
- [55] G. C. Le Goff, J. Lee, A. Gupta, W. A. Hill, P. S. Doyle, *Adv. Sci.* **2015**, *1500149*.

- [56] L. Treiber, W. Owens, *Soc. Pet. Eng. J.* **1972**, *12*, 531.
- [57] X. Shi, R. Rosa, A. Lazzeri, *Langmuir* **2010**, *26*, 8474.
- [58] R. Shukla, P. Ranjith, A. Haque, X. Choi, *Fuel* **2010**, *89*, 2651.
- [59] I. M. Banat, A. Franzetti, I. Gandolfi, G. Bestetti, M. G. Martinotti, L. Fracchia, T. J. Smyth, R. Marchant, *Appl. Microbiol. Biotechnol.* **2010**, *87*, 427.
- [60] R. S. K. Lam, J. M. Charnock, A. Lennie, F. C. Meldrum, *CrystEngComm* **2007**, *9*, 1226.
- [61] K. Sawada, *Pure Appl. Chem.* **1997**, *69*, 921.
- [62] N. Koga, Y. Z. Nakagoe, H. Tanaka, *Thermochim. Acta* **1998**, *318*, 239.
- [63] J. Xu, C. Yan, F. Zhang, H. Konishi, H. Xu, H. H. Teng, *Proc. Natl. Acad. Sci. USA* **2013**, *110*, 17750.
- [64] D. C. Green, R. Boston, S. Glatzel, M. R. Lees, S. C. Wimbush, J. Potticary, W. Ogasawara, S. R. Hall, *Adv. Funct. Mater.* **2015**, *25*, 4700.
- [65] B. Purgstaller, V. Mavromatis, A. Immenhauser, M. Dietzel, *Geochim. Cosmochim. Acta* **2016**, *174*, 180.
- [66] K. Rae Cho, Y.-Y. Kim, P. Yang, W. Cai, H. Pan, A. N. Kulak, J. L. Lau, P. Kulshreshtha, S. P. Armes, F. C. Meldrum, J. J. De Yoreo, *Nat. Commun.* **2016**, *7*, 10187.
-